The low-temperature highly correlated quantum phase in the charge-density-wave 1T-TaS$_2$ compound

Marie Kratochvilova[1,2], Adrian D. Hillier[3], Andrew R. Wildes[4], Lihai Wang[5], Sang-Wook Cheong[5] and Je-Geun Park[1,2]

A prototypical quasi-2D metallic compound, 1T-TaS$_2$ has been extensively studied due to an intricate interplay between a Mott-insulating ground state and a charge-density-wave order. In the low-temperature phase, 12 out of 13 Ta^{4+} 5d-electrons form molecular orbitals in hexagonal star-of-David patterns, leaving one 5d-electron with $S = \frac{1}{2}$ spin free. This orphan quantum spin with a large spin-orbit interaction is expected to form a highly correlated phase of its own. And it is most likely that they will form some kind of a short-range order out of a strongly spin-orbit coupled Hilbert space. In order to investigate the low-temperature magnetic properties, we performed a series of measurements including neutron scattering and muon experiments. The obtained data clearly indicate the presence of the short-ranged phase and put the upper bound on ~0.4 μ$_B$ for the size of the magnetic moment, consistent with the orphan-spin scenario.

INTRODUCTION

The instability of charge density waves (CDW) found in low-dimensional electron systems of layered materials has attracted enormous attention recently. 1T-TaS$_2$ is a prototypical quasi-2D metallic compound with a strong electron-phonon coupling responsible often for CDW instabilities. Upon cooling, it undergoes a series of first-order phase transitions to CDW, Mott and superconducting phases (see e.g., ref. [1] and references therein).

1T-TaS$_2$ bulk crystal has a lamellar structure, with each layer composed of a triangular lattice of Ta atoms which is then sandwiched by S atoms in an octahedral TaS$_6$ coordination with a weak Van der Waals bonding between the layers. Above ~540 K, the structure is unmodulated trigonal with *P-3m1* symmetry; below which the triangular lattice exhibits a series of structural modulations.[2, 3] First, an incommensurate CDW phase sets in at T ~ 540 K. Upon further cooling, the structure changes to a nearly commensurate phase at T_{nCDW} ~ 350 K. Finally, the material turns into a Mott insulating phase with in-plane $\sqrt{13} \times \sqrt{13}$ superlattice distortion, which coexists with a commensurate CDW phase below T_{CDW} ~180 K. Superconductivity emerges in 1T-TaS$_2$ below ~2 K by introducing disorders.[4] Recent angle-resolved photoemission spectroscopy experiments suggest that the melted Mott state and the superconductivity coexist in real space[5] providing better understanding of the interplay between electron correlation, charge order, and superconductivity. Unlike other Mott insulators, the CDW superlattices play the role of localization centers in the ground state of 1T-TaS$_2$.

According to the current understanding, the CDW phase is composed of molecular orbitals of 13 Ta atoms, forming a hexagonal pattern of so-called David-star clusters. As proposed more than three decades ago,[6] each Ta^{4+} of 1T-TaS$_2$ provides one 5d electron, and thus there are 13 5d-electrons per each David star. Out of these 13 electrons, 12 electrons form 6 covalent bonds and so they become inactive both electrically and magnetically, leaving one 5d-electron localized well inside the David star. This orphan electron provides $S = \frac{1}{2}$ per each David star, and becomes localized at low temperatures ($T < 60$ K) in the center of the David star.[7, 8] We note that in the 2D quantum triangular lattice systems, a combination of reduced dimensionality, geometric frustration, and a small spin value significantly enhances quantum fluctuations, which can easily induce exotic quantum states. In contrast to other $S = \frac{1}{2}$ triangular systems showing rich phase diagrams such as CuRE_2Ge$_2$O$_8$,[9] Ba$_3$CoSb$_2$O$_9$,[10] and others,[11, 12] there is no apparent magnetic ordering in the insulating ground state of 1T-TaS$_2$ down to the lowest measured temperatures.

Instead, a commensurate CDW phase forms most likely through Mott–Hubbard physics with possibly intricate electron–phonon and electron-electron interactions.[13] This then leaves the orphan spin ($S = 1/2$) with a large spin-orbit interaction in the low-temperature CDW phase. How this orphan quantum spin behaves at low temperatures has been at the focus of current attention and hence extensively studied both theoretically[7, 8, 14] and experimentally.[13, 15–17] There is even a suggestion that it may form a highly correlated, "hidden" phase of its own and just recently,[18] 1T-TaS$_2$ was suggested to be considered as a quantum spin liquid. Yet, none of the experimental works focused directly on the investigation of this low-temperature phase with a very recent exception.[19] It is thus interesting to ask whether some kind of a short-range ordering would be formed out of the strongly spin-orbit coupled Hilbert space, in which a magnetic moment $\mu = g_s\sqrt{(S(S+1))}/13$ μ$_B$ ~ 0.13 μ$_B$ for $S = \frac{1}{2}$ per each David star is expected.

In this work, we tried to address the question of a possible low-temperature correlated phase. For this, we have performed extensive bulk measurements, polarized neutron diffraction and μSR studies covering a wide range of time scales and spatial

[1]Center for Correlated Electron Systems, Institute for Basic Science, Seoul 08826, Korea; [2]Department of Physics and Astronomy, Seoul National University, Seoul 08826, Korea; [3]ISIS, STFC, Rutherford Appleton Laboratory, Didcot OX11 0QX, UK; [4]Institut Laue-Langevin, 156X, 38042 Grenoble Cedex, France and [5]Rutgers Center for Emergent Materials and Department of Physics and Astronomy, Rutgers University, Piscataway, NJ 08854, USA
Correspondence: Marie Kratochvilova (kratm6bm@snu.ac.kr) or Je-Geun Park (jgpark10@snu.ac.kr)

np̃j

The highly correlated quantum phase in 1T-TaS$_2$
M Kratochvilova et al.

2

resolution. μSR and diffuse neutron scattering are ideal experimental techniques for investigating the weak magnetic signals and providing information on a correlation length of magnetic order, respectively.

RESULTS

We measured the magnetic susceptibility in the temperature range of 2–400 K with magnetic field applied along the hexagonal basal plane using several samples from different batches (see Fig. 1a, b). Diamagnetic signal dominates the data from high temperatures down to ~50 K, except for intermediate interruptions by two jumps at T_{CDW} and T_{nCDW}, which signal a transition from the commensurate to the nearly commensurate phase and then to another incommensurate phase, respectively. While the transition to the incommensurate phase takes place at T_{nCDW} ~355 K, the transition at T_{CDW} shows a remarkable hysteresis as shown in the inset of Fig. 1b and reaches values of ~220 K upon warming and ~160 K upon cooling. Interestingly, all the $\chi(T)$ curves exhibit a strong paramagnetic Curie–Weiss tail below ~50 K, suggesting that some kind of a short-range correlation might exist

at low temperatures. Magnetic impurities were excluded as a source of the low-temperature Curie contribution, considering the fact that we consistently observed a comparable low-temperature tail of almost similar magnitude for all the five samples prepared from raw materials of different purity. We also note that the Curie constant is too high to be explained purely by an extrinsic effect.[20] Our estimate of ~8 μB/f.u. for the impurity moments is a too big a value if we adopt the impurity based explanation. All the known structure phases of the 1T-TaS$_2$ compound are summarized in Table 1.

The magnetic susceptibility was fitted using the following equation with a diamagnetic/Pauli paramagnetic contribution χ_0 and a Curie-type paramagnetic contribution in the temperature region from 2 to 200 K;

$$\chi = \frac{C}{T - \theta} + \chi_0,\tag{1}$$

where C is the Curie constant and θ is the paramagnetic temperature. The temperature dependence of the inverse magnetic susceptibility and the respective fits are shown in Fig. 1d. Parameters of the Curie–Weiss fit are also summarized in Table
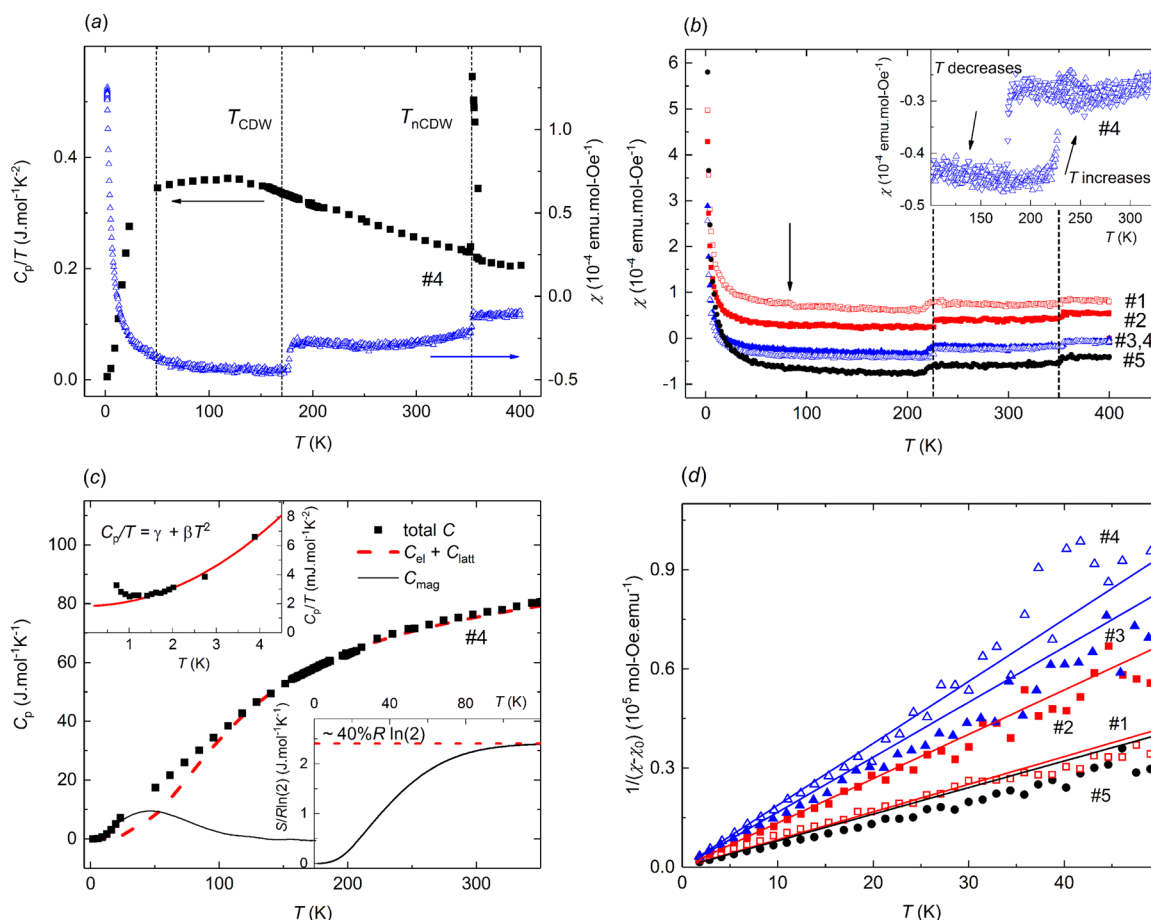

Fig. 1 Magnetic and thermodynamic properties of 1T-TaS$_2$ **a** Comparison of the temperature dependence of specific heat and magnetic susceptibility of the 1T-TaS$_2$ single crystal #4 measured upon cooling. The dashed lines mark the position of the transitions at T_{CDW} ~160 K and T_{nCDW} ~355 K and the temperature ~50 K, below which an upturn in both data sets is observed. **b** The temperature dependence of the magnetic susceptibility measured on five 1T-TaS$_2$ single crystals in magnetic field of 0.2 T upon warming. The *dashed lines* mark the transition at T_{CDW} ~ 210 K and T_{nCDW} ~ 355 K. The inset shows the blown-up picture of the data near T_{CDW} for the single crystal #4 measured upon cooling and warming. **c** Total specific heat of the 1T-TaS$_2$ single crystal #4 (*closed squares*) with the estimated lattice and electronic (*dashed line*) contribution and the magnetic (*solid line*) contribution. The low-temperature region of the specific heat is shown in the upper inset. The *red line* is the Sommerfeld fit to the data as given by the equation $C_p/T = \gamma + \beta T^2$. The magnetic entropy is shown in the lower inset. Approximately 40% of the theoretical maximum entropy (5.76 J mol^{-1} K^{-1}) is released as marked by the *red dashed line*. **d** The temperature dependence of the inverse magnetic susceptibility of the five 1T-TaS$_2$ single crystals from **b** and their respective Curie–Weiss fits

The highly correlated quantum phase in 1T-TaS$_2$
M Kratochvilova et al.

npj

3

Table 1. 1T-TaS$_2$ phase diagram

Temperature	Phase
$T > 540$ K	Trigonal with P-3$m1$ symmetry
540 K $> T >$ 355 K	Incommensurate
355 K $> T >$ 160 K	Nearly commensurate (upon cooling)
160 K $> T$	Commensurate Mott insulator
60 K $> T$	Localization of the free electron

S1 in the Supplemental Material. The single crystals #1 and #2 are not diamagnetic down to ~50 K, probably due to a small presence of the 2H-polymorph in the samples (discussed in the Supplemental Material) which reveals itself by a tiny bump at ~75 K corresponding to the CDW transition[21] (marked by the arrow in Fig. 1b). We note that the size of the effective magnetic moment and the Curie–Weiss temperature (θ_{CW}) is similar for all the measured samples with $\mu_{eff} \sim 0.08$ μ_B/f.u. and $\theta_{CW} \sim 0.02$ K, respectively. Therefore, we observe ~50% reduction of the observed μ_{eff} value from the expected spin-only value of ~0.13 μ_B for one magnetic moment per each David star. On the other hand, the small value of θ indicates weak magnetic correlations present at low temperatures.

In order to investigate the thermodynamic nature of the transitions, we also measured the specific heat. The specific heat collected upon cooling from 400 down to 0.7 K is shown in Fig. 1a in comparison to the magnetic susceptibility data. In accordance with the magnetic susceptibility, the specific heat reveals a typical first-order transition from the incommensurate to the nearly commensurate phase at $T_{nCDW} \sim 355$ K. However, we failed to observe any lambda-like peak signifying the first-order transition into the commensurate phase in contrast to the behavior of $\chi(T)$ measured on the identical sample. Instead, the C_p/T (T) curve shows a moderate decrease followed by a clear change of the slope at $T_{CDW} \sim 150$ K. Similar discontinuous decrease/increase (depending on the rise/decrease of temperature) of the specific heat in the vicinity of T_{CDW} was observed in the case of incommensurate-to-commensurate transition in 2 H-TaSe$_2$.[22] Moreover, a discontinuity in the specific heat of 1T-TaS$_2$ was predicted by the calculation based on the Born von Karman model.[23] Upon further cooling, the C_p/T (T) curve reveals a sharp drop at ~50 K, which may be related to the upturn in the magnetic susceptibility at a similar temperature range.

The high-temperature specific heat data shown in Fig. 1c were modeled by the Debye equation. The phonon contribution can be written as

$$C_{ph} = 9NR \left(\frac{T}{\theta_D} \right)^3 \int_0^{\theta_D/T} \frac{x^4 e^x dx}{(e^x - 1)^2},$$

(2)

Our analysis produces the following parameters for the best fit: the Debye temperature of $\theta_D \sim 450$ K, the Sommerfeld coefficient of $\gamma = 1.84$ mJ mol^{-1} K^{-2}, and the coefficient $\beta = 0.31$ mJ mol^{-1} K^{-4} as shown in the upper inset of Fig. 1c. We note that these values correspond rather well to those obtained from the previous experiment carried on powder sample.[24] Interestingly enough, the value of γ is close to the theoretical value of 3.56 mJ mol^{-1} K^{-2} from DFT calculations.[25] We note that $C_p(T)$ shows a modest increase below ~1 K, indicating some kind of residual entropy still remaining at very low temperatures.

After subtracting off the estimated lattice and electron contributions, we can get a broad hump centered at ~50 K in the magnetic heat capacity C_{mag}, indicative of some kind of short-ranged order. Integrating the peak area yields an entropy released by this correlated phase, which is ≈40% of the theoretical maximum entropy $R\ln(2) = 5.76$ J mol^{-1} K^{-1}.
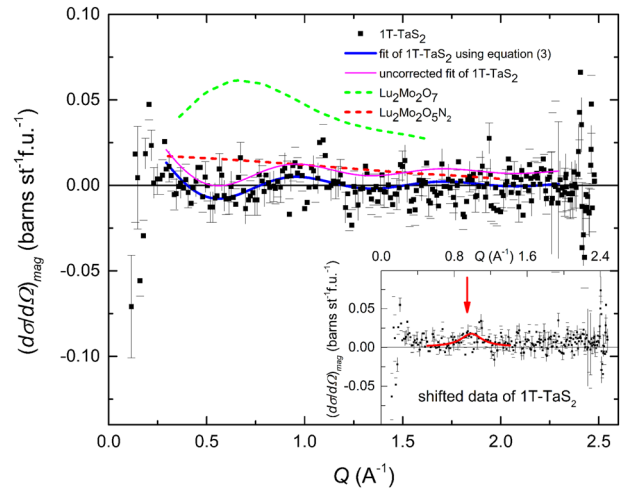

Fig. 2 The magnetic scattering cross section of 1T-TaS$_2$ at 1.5 K. The inset shows the shifted data (see the text for details) and the Lorentz fit of the bump located at $Q \sim 0.9$ Å^{-1}, while the main figure presents the original data together with the fit and the data measured on the Lu$_2$Mo$_2$O$_7$ compound. Vertical error bars represent 1σ s.d. counting statistics. (Fig. 2 shows the data of the Lu$_2$Mo$_2$O$_7$ compound taken from ref. 27 with permission. Copyrighted by the American Physical Society)

When taken together, the analysis of the Curie–Weiss fits, the low-temperature specific heat and the magnetic susceptibility provided clear evidence in support of the presence of a low-temperature correlated phase. In order to get a more direct insight into the low-temperature ground state of 1T-TaS$_2$, we performed neutron scattering and muon spin relaxation experiments. Figure 2 shows the magnetic scattering data ($d\sigma/d\Omega)_{mag}$ of the 1T-TaS$_2$ compound. Although the signals are relatively weak, closer inspection of the data reveals a bump emerging in the Q–range from 0.7 to 1.2 Å^{-1} (for more information about the signal quality, see the Supplemental Material). To emphasize the possible presence of a broad peak marked by the *red arrow* in the inset of Fig. 2, the original data were shifted upwards by a factor of 0.0075 barn st^{-1} f.u.$^{-1}$.

We can model the data by the expression for the magnetic neutron-scattering differential cross section,

$$\left(\frac{d\sigma}{d\Omega} \right)_{mag} = \frac{2}{3} \left(\frac{\gamma_n r_0}{2} \right)^2 f^2(\vec{Q}) g_s^2 S(S+1) \times$$

$$\left[1 + \sum_{n=1}^{\infty} Z_n \frac{\langle S_0 \cdot S_n \rangle}{S(S+1)} \frac{\sin QR_n}{QR_n} \right] - \left(\frac{d\sigma}{d\Omega} \right)_{bkg},$$

(3)

which is valid in the case of a disordered magnetic configuration. The background term $\left(\frac{d\sigma}{d\Omega} \right)_{bkg} = 0.0075$ barn st^{-1} f.u.$^{-1}$ was added into the Eq. (3) to compensate the systematic errors which play an important role in our data with the low signal-to-noise ratio. Details are discussed in the Supplemental Material. Using the formula, we can calculate the average spin-spin correlation functions $\langle S_0 \cdot S_n \rangle$ for the nth nearest neighbor radial shell around a central Ta atom at the origin. Here, γ_n is the neutron gyromagnetic ratio, r_0 is the classical electron radius and $f(Q)$ is the magnetic form factor of the magnetic species used considering Ta^{4+} in our case,[26] $g^2 S(S+1)$ is the squared magnetic moment and Z_n and R_n are the coordination number and radial distance of the nth nearest-neighbor shell, respectively. For a paramagnetic system without any spin-spin correlations, the Q-dependence of magnetic cross section corresponds straightforwardly to the evolution of the absolute squared magnetic moment per atom.

To define reasonable limits for the fitting parameters, we compared our data to those measured on the Lu$_2$Mo$_2$O$_7$ oxide

npj

The highly correlated quantum phase in 1T-TaS$_2$
M Kratochvilova et al.

4

and the Lu$_2$Mo$_2$O$_5$N$_2$ oxynitride.[27] We recall that in our orphan spin scenario the spin moment is expected to be localized in the respective David star consistent with what one would expect in the low-temperature CDW phase. The bump in the oxide data taken after ref. [27] was previously modeled by taking into account the nearest- and the next-nearest-neighbor correlations $\langle S_0 \cdot S_1 \rangle = -0.029$ and $\langle S_0 \cdot S_2 \rangle = -0.056$, respectively, proving the presence of the static short-range molybdenum spin correlations (*green dashed line* in Fig. 2). On the other hand, the oxynitride data follow the $f^2(Q)$ dependence with zero $\langle S_0 \cdot S_i \rangle$ correlations (*red dashed line* in Fig. 2). Similar fit of our neutron data on 1T- TaS$_2$ produces the effective magnetic moment of 0.11 μ_B/f.u., representing an upper bound for the magnetic moment of the orphan spins.

As shown in ref. [28], double layers are connected by the *c*-stacking vector across the hexagonal sheets. As a result, the low-temperature phase is commensurate only in the basal plane and not along the *c*-axis because the stacking order established along the *c*-axis is not periodic. Related to this issue, two types of stacking patterns–screw and repetitive–have been previously observed in the ratio ~1:2.7 for 1T-TaS$_2$. Due to the large spatial extent of the David star, the nearest neighbors that are expected to contribute to the magnetic cross section are located across the hexagonal layers and not within them. Indeed, assuming that the crucial correlations take place only within the CDW layer, the fit cannot describe satisfactorily the data (shown in Fig. S2 in the Supplemental Material). Therefore, the three-dimensional character of the electronic correlations at low temperatures has to be considered. This result is indeed in good agreement with the recent experimental and theoretical studies, which suggested the importance of interlayer coupling.[14, 29–31] In order to describe the broad peak well by the expression (3), we had to include interactions among the nearest ($r_1 = 5.90$ Å, $Z_1 = 1$) and the next-nearest-neighbor ($r_2 = 8.29$ Å, $Z_2 = 1$) in the repetitive stacking and the next-nearest-neighbor ($r_2' = 6.79$ Å, $Z_2' = 1$) in the screw stacking with respect to their ratio, as depicted in Fig. 3.

The best fit to the data by the Eq. (3) was obtained for the effective magnetic moment of 0.4 ± 0.05 μ_B ($\approx 300\%$ of the expected magnetic moment per each David star) and for the average correlations $\langle S_0 \cdot S_1 \rangle = -0.07 \pm 0.05$, $\langle S_0 \cdot S_2 \rangle = 0.17 \pm 0.10$, $\langle S_0 \cdot S_2 \rangle' = 0.39 \pm 0.16$, respectively (*solid blue line* in Fig. 2). The *solid magenta line* represents the fit without the correction on the background term. The magnetic moment is higher compared to the expected $\mu \sim 0.13$ μ_B value of the magnetic moment per each David star; however, it is necessary to keep in mind that the values of the fitted parameters represent the upper limit. Also, the values and error bars of the average correlations need to be understood in terms of very low signal-to-noise ratio. The dominant correlation is weakly antiferromagnetic, while the
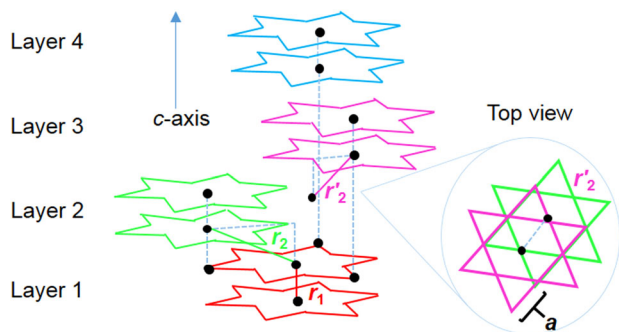
second-nearest neighbor correlations are more robust and ferromagnetic; further correlations among more distant David-star patterns can be neglected. Here we note that there are considerable nearest and next-nearest $\langle S_0 \cdot S_i \rangle$ correlations with opposite signs. Interestingly, the ferromagnetic nature of $\langle S_0 \cdot S_i \rangle$ for $i = 2$ corresponds to the positive value of the Curie–Weiss temperatures θ_{CW} obtained from the magnetization measurement, hinting at subtle ferromagnetic correlations.

In order to study further the short-range magnetic order, we carried out the zero-field (ZF) muon-spin relaxation study from 5 up to 250 K. The ZF spectra can be modeled using the following expressions:

$$G_z(t) = a_i G_{KT}(t) \times G_{mag}(t) + a_{bg}, \quad (4)$$

$$G_{KT}(t) = \frac{1}{3} + \frac{2}{3}\left(1 - \sigma^2 t^2\right) exp\left(-\frac{\sigma^2 t^2}{2}\right), \quad (5)$$

$$G_{mag}(t) = exp(-\lambda t), \quad (6)$$

where a_i and a_{bg} are the initial and background asymmetries, respectively. Eq. (5) describes the static Gaussian Kubo–Toyabe function, whereas σ is the nuclear depolarization rate. $G_{mag}(t)$ from Eq. (6) is the magnetic part of the relaxation function, which represents the muon-spin relaxation rate λ from the dynamic magnetic fields associated with fluctuating atomic spins. Consistent with the neutron experiment, we observe a sign of the presence of a low-temperature short-ranged magnetic ordering in the asymmetry spectra compared to high temperatures as shown in Fig. 4a, b. The asymmetry spectra can be characterized by the typical Kubo–Toyabe evolution and no pronounced qualitative differences among the spectra are observed for various temperatures (the spectra measured at 5 and 250 K are shown for comparison).

To suppress the nuclear contribution to the muon asymmetry function, small LF field of 5 mT was applied in a direction parallel to the muon polarization; which is sufficient to fully decouple the muons from the relaxation channel. The effect of the applied longitudinal field also indicates that the magnetism is dynamic in the investigated temperature range (see Fig. S3 in the Supplemental Material). Fig. 4c–e summarizes the results of the Kubo–Toyabe fit over the whole temperature range for the fitting parameters a_i, λ and σ. The ZF run of the initial asymmetry parameter shown in Fig. 4c remains temperature-independent down to ~50 K, where the asymmetry starts to decrease slightly and at the lowest measured temperature of 5 K. This change points to the onset of a short-range magnetic order. The relaxation rate λ in Fig. 4d shows a slight increase below ~50 K, implying that this extra relaxation might indicate additional internal magnetic fields. This result by itself is not conclusive as the effect is very weak, in agreement with the recent µSR measurements performed by Klanjšek et al.[19]; however, together with the bulk and neutron data it forms a comprehensive picture about the low-temperature state in 1T-TaS$_2$. The depolarization rate σ in Fig. 4e reveals an interesting temperature evolution. Upon warming, it starts to deviate from the constant value at ~100 K, which is probably a sign of the muons diffusion, and a minimum of σ is observed at ~210 K. This value coincides well with the temperature T_{CDW} ~210 K (upon warming) of the commensurate CDW transition obtained from the magnetic susceptibility measurement.

Fig. 3 CDW structure and interplane stacking in 1T-TaS$_2$. The lattice parameter $a = 3.36$ Å is depicted in the top view. In the case of the repetitive stacking with the nearest-neighbor distances $r_1 = 5.90$ Å and $r_2 = 8.29$ Å only double layers one and two alternate while the screw stacking with the nearest-neighbor distances r_1 and $r_2' = 6.79$ Å is formed by double layers one to four

DISCUSSION

With those data from the specific heat and the magnetic susceptibility, we can calculate the Sommerfeld-Wilson ratio. The

The highly correlated quantum phase in 1T-TaS$_2$
M Kratochvilova et al.

npj

5

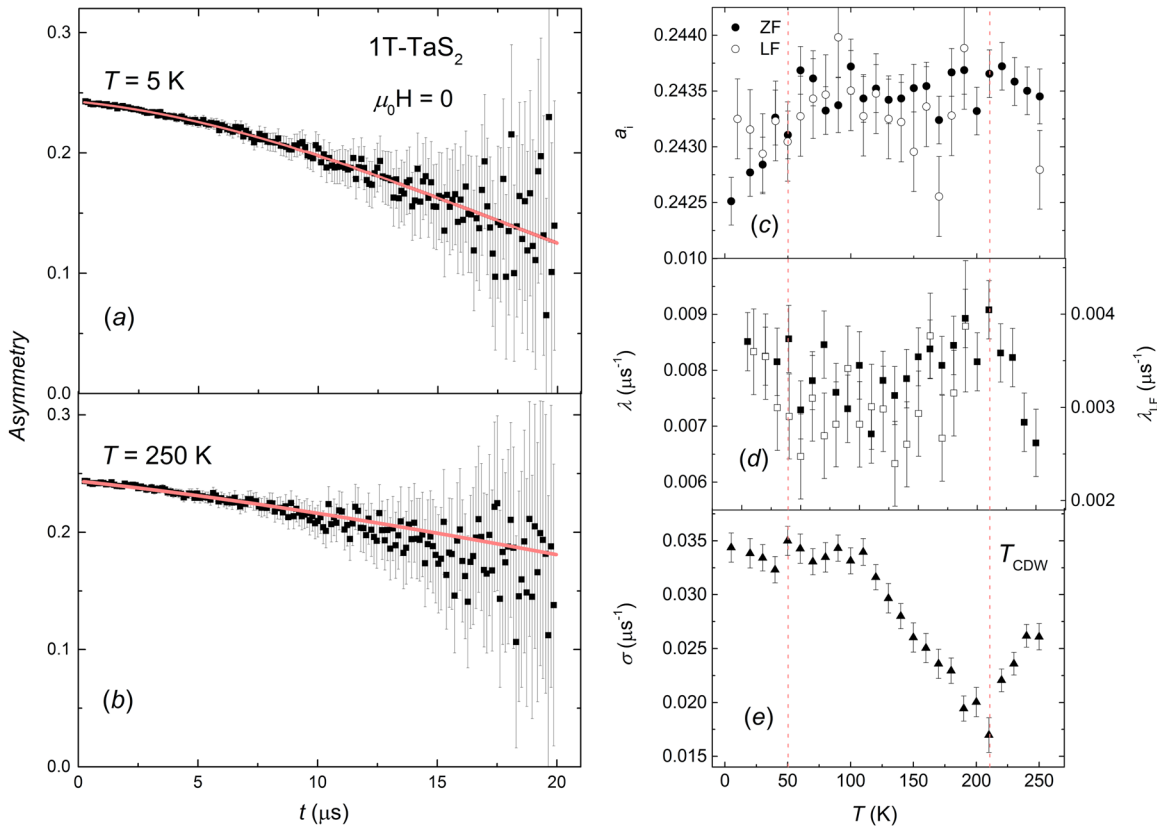**Fig. 4** The μSR data of 1T-TaS$_2$. The ZF μSR asymmetry spectra of 1T-TaS$_2$ are measured at **a** 5 K, and **b** 250 K; the red line represents the fit described in the text. Vertical error bars represent 1σ s.d. counting statistics. Temperature dependence of the initial asymmetry both in the ZF and LF mode **c**, the relaxation rate **d**, and the nuclear depolarization rate **e**, taken from the fit described in the text. The vertical error bars for a_i, λ, and σ are from fits. The *dashed line* at 210 K marks the position of the transition into the CDW state upon cooling. The *dashed line* at ~50 K marks the temperature where the trend of the three parameters changes which might be associated with the possible onset of the magnetic short-range order at low temperatures

ratio is given as

$$R_w = \frac{4\pi^2 k_B^2}{3(g\mu B)^2} \frac{\chi_0}{\gamma}. \tag{7}$$

With $\chi_0 = 5 \cdot 10^{-4}$ emu mol^{-1} as obtained at the lowest measured temperature $T = 1.8$ K and for $\gamma = 1.84$ mJ mol^{-1} K^{-2} using the identical sample #4, we get $R_W \sim 2$ ($R_W = 1$ for the free electron gas) indicating the presence of considerable electronic correlations at low temperatures.

Another remarkable feature in $\chi(T)$ is the absolute size of the jumps $\Delta\chi_1$ and $\Delta\chi_2$ that is consistently seen for all the measured samples (see Table S1 in the Supplemental Material) although the absolute values of $\chi(T)$ are strongly sample-dependent due to different susceptibility term χ_0. From the ratio of the jumps it is possible for us to estimate the relative ratio of the CDW-induced energy gaps as

$$\frac{\Delta\chi_1}{\Delta\chi_2} = \frac{\Delta N(T_{CDW})}{\Delta N(T_{nCDW})} \sim 1.5, \tag{8}$$

where ΔN is the electron density of states. The early tunneling experiments on 1T-TaS$_2$[32, 33] were carried out to investigate the size of the charge gaps directly and reported somewhat a larger ratio of ~2.5 for charge gap of ~10 eV at T_{CDW} and 0.4 eV at T_{nCDW}. Later, it was shown that the gap opening at the Fermi level is related to the Mott localization in the commensurate CDW phase.[34] Turning to the question on the low-temperature phase, both the magnetic susceptibility and the specific heat suggest the presence of a correlated phase; another support for this scenario

can be found in the neutron data that show a clear bump at a finite Q value. The position of the bump in the diffuse magnetic scattering of 1T-TaS$_2$ is Q ~ 0.9 Å^{-1}, close to $2\pi/r'_2$, where $r'_2 = 6.79$ Å is the next nearest-neighbor distance across the screw stacking layers. As the respective correlation for this neighbor distance is positive, the Q-position implies ferromagnetic correlations between pairs of spins across the hexagonal layers. The correlation length extracted from the full width at half maximum (~0.285 ± 0.060 Å^{-1}) of the bump (see the Lorentz fit shown in the inset of Fig. 2) is L ~22 Å, which roughly corresponds to $4r_1$. Thus, we conclude that correlated domains show a large spatial extent almost over two David-star patterns and across four hexagonal sheets.

Finally, the temperature evolution of the parameters a_i and λ obtained by μSR measurement reveals a change of slope below ~50 K. This temperature scale seems to have a physical significance as it corresponds to the abrupt changes in the temperature evolution of specific heat and magnetic susceptibility. Interestingly, a spontaneous ordering into the hidden state in 1T-TaS$_2$ was observed below 100 K after an application of the sub-35-fs laser pulse under non-equilibrium conditions.[35] Our μSR experiment shows a subtle change in the temperature evolution of the relaxation rate and initial asymmetry value below 50 K, which can be taken as a signature of a low-temperature correlated phase in accordance with the neutron and bulk measurements.

To sum up, we have performed complementary specific heat, magnetization, neutron diffraction, and μSR measurements of 1T-

npj

The highly correlated quantum phase in 1T-TaS$_2$
M Kratochvilova et al.

6

TaS$_2$ to study the nature of the low-temperature hidden order within the commensurate CDW phase. All the results presented here consistently offer evidences of the "orphan spin" scenario with $S = \frac{1}{2}$ moments localized in the centers of the David stars, albeit with a somewhat higher value of the effective magnetic moment as compared to the proposed ~0.13 μ_B per David star. Our results support also the important role of the interlayer correlations in the electronic structure of 1T-TaS$_2$ in line with theoretical studies.[30]

METHODS

Polycrystals and single crystals of 1T-TaS$_2$ was prepared by the solid-state high-temperature reaction of initial elements and by the chemical vapor transport method, respectively (for details of the synthesis, see the Supplemental Material). The samples were characterized by X-ray diffraction (Bruker XRD D8 Discover for powder and Rigaku XtaLAB P200 for single crystals) and confirmed to have the trigonal crystal structure crystallizing in the P-3m1 space group (see Fig. S1 in the Supplemental Material). The magnetization and heat capacity measurements were carried out using commercial set-ups: MPMS-3 EverCool (Quantum Design, USA) and PPMS-9 equipped with the low-temperature He3 option (Quantum Design, USA).

Polarized diffuse neutron scattering was performed on D7 at Institut Laue-Langevin using 4.2 g of sample placed in a double-wall Al cylinder can and incident energy $E_i = 3.5$ meV ($\lambda = 4.8$ Å). The temperature was kept at 1.5 K during the whole experimental time. The instrument background was estimated by adding the scattering from an empty and a cadmium-filled sample holder, weighted by the sample transmission. This was subtracted from the data. The data were then subsequently corrected for polarization efficiency using the scattering from amorphous quartz. Vanadium was measured to estimate detector efficiency and to put the data on an absolute scale. Equal time was spent on measuring the scattering along the X, Y, and Z directions. The nuclear, magnetic, and nuclear spin-incoherent scattering cross sections were separated as a function of both momentum and energy transfer using the 6-point 'xyz'-polarization analysis.[36] The non-spin-flip and spin-flip scattering along each direction was measured with a time ratio of 1:8.

μSR spectra were measured using the EMU spectrometer at the ISIS Facility, Rutherford Appleton Laboratory, U.K. in the temperature range from 5 to 250 K using a Close Cycle Refrigerator. The sample of the mass of ~20 g was enclosed in an Al sample holder. Any exposed Al to the beam was covered by a silver mask (dia. 30 mm) with a 30 μm mylar window for the muons to pass through before entering the sample. The decay-positron asymmetry function was measured as a function of time, in the zero-field (ZF) regime to examine the unperturbed magnetic behavior and in the longitudinal field (LF) of 5 mT.

Data availability

The data that support the findings of this study are available from the corresponding author upon reasonable request.

AUTHOR CONTRIBUTIONS

J.G.P. conceived the idea and supervised the project. M.K. carried out all the experiments: the neutron scattering experiments were done together with A.W. while muon experiments were done with A.H. L.W. and S.W.C. prepared the sample. M.K. and J.G.P. wrote the manuscript with contributions from all the other authors.

REFERENCES

1. Sipos, B. *et al.* From Mott state to superconductivity in 1T-TaS$_2$. *Nat. Mat.* **7**, 960–965 (2008).
2. Wilson, J. A. *et al.* Charge-density waves and superlattices in the metallic layered transition metal dichalcogenides. *Adv. Phys* **24**, 117–201 (1975).
3. Spijkerman, A. *et al.* X-ray crystal-structure refinement of the nearly commensurate phase of 1T–TaS$_2$ in (3 + 2)-dimensional superspace. *Phys. Rev. B* **56**, 13757–13767 (1997).
4. Xu, P. *et al.* Superconducting phase in the layered dichalcogenide 1T-TaS$_2$ upon inhibition of the metal-insulator transition. *Phys. Rev. B* **81**, 172503 (2010).
5. Ang, R. *et al.* Real-Space Coexistence of the Melted Mott State and Super-conductivity in Fe-Substituted 1T-TaS$_2$. *Phys. Rev. Lett.* **109**, 176403 (2012).
6. Fazekas, P. & Tosatti, E. Electrical, structural and magnetic properties of pure and doped 1T-TaS$_2$. *Philos. Mag. B* **39**, 229–244 (1979).
7. Rossnagel, K. & Smith, N. V. Spin-orbit coupling in the band structure of reconstructed 1T–TaS$_2$. *Phys. Rev. B* **73**, 073106 (2006).
8. Gan, L.-Y. *et al.* Strain tuning of the charge density wave in monolayer and bilayer 1T-TaS$_2$. *Phys. Chem. Chem. Phys.* **18**, 3080–3085 (2016).
9. Cho, H. *et al.* Properties of spin-1/2 triangular-lattice antiferromagnets CuY$_2$Ge$_2$O$_8$ and CuLa$_2$Ge$_2$O$_8$. *Phys. Rev. B* **95**, 144404 (2017).
10. Koutroulakis, G. *et al.* Quantum phase diagram of the S = 1/2 triangular-lattice antiferromagnet Ba$_3$CoSb$_2$O$_9$. *Phys. Rev. B* **91**, 024410 (2015).
11. Rawl, R. *et al.* Ba$_8$CoNb$_6$O$_{24}$: A spin-1/2 triangular-lattice Heisenberg antiferromagnet in the two-dimensional limit. *Phys. Rev. B* **95**, 060412(R) (2017).
12. Zvyagin, S. A. *et al.* Magnetic excitations in the spin-1/2 triangular-lattice antiferromagnet Cs$_2$CuBr$_4$. *New. J. Phys.* **17**, 113059 (2015).
13. Zhu, X. *et al.* Classification of charge density waves based on their nature. *PNAS* **112**, 2367–2371 (2015).
14. Bovet, M. *et al.* Interplane coupling in the quasi-two-dimensional 1T–TaS$_2$. *Phys. Rev. B* **67**, 125105 (2003).
15. Yoshida, M. *et al.* Memristive phase switching in two-dimensional 1T-TaS$_2$ crystals. *Sci. Adv* **1**, 1–6 (2015).
16. Ritschel, T. *et al.* Orbital textures and charge density waves in transition metal dichalcogenides. *Nat. Phys* **11**, 328–331 (2015).
17. Cho, D. *et al.* Interplay of electron-electron and electron-phonon interactions in the low-temperature phase of 1T-TaS$_2$. *Nat. Comm* **7**, 10453 (2015).
18. Law, K. T. & Lee, P. A. Is 1T-TaS$_2$ a quantum spin liquid? Preprint at https://arxiv.org/abs/1704.06157 (2017).
19. Klanjsek, M. *et al.* A new high-temperature quantum spin liquid with polaron spins. Preprint at https://arxiv.org/abs/1704.06450 (2017).
20. DiSalvo, F. J. *et al.* Paramagnetic moments and localization in 1T-TaS$_2$. *Phys. Rev. B* **22**, 4241–4246 (1980).
21. Tidman, J. P. *et al.* The phase transition in 2H-TaS$_2$ at 75 K. *Phil. Mag.* **30**, 1191–1194 (1974).
22. Craven, R. A. & Meyer, S. F. Specific heat and resistivity near the charge-density-wave phase transitions in 2H–TaSe$_2$ and 2H–TaS$_2$. *Phys. Rev. B* **16**, 4583–4593 (1977).
23. Balaguru Rayappan, J. B. *et al.* Thermal properties of 1T-TaS$_2$ at the onset of charge density wave states. *Phys. B* **405**, 3172–3175 (2010).
24. Benda, J. A. Optical, electrical-transport, and heat-capacity studies of solid-solutions Ti$_x$Ta$_{1-x}$S$_2$, Zr$_x$Ta$_{1-x}$S$_2$, and Ti$_x$Nb$_{1-x}$Se$_2$. *Phys. Rev. B* **10**, 1409–1420 (1974).
25. Yan-Bin, Q. *et al.* Anisotropic properties of TaS$_2$. *Chin. Phys.* **16**, 3809–3814 (2007).
26. Kobayashi, K. *et al.* Radial integrals for the magnetic form factor of 5d transition elements. *Acta Cryst. A* **67**, 473–480 (2011).
27. Clark, L. *et al.* From spin glass to quantum spin Liquid ground states in molybdate pyrochlores. *Phys. Rev. Lett.* **113**, 117201 (2014).
28. Ishiguro, T. & Sato, H. Electron microscopy of phase transformations in 1T-TaS$_2$. *Phys. Rev. B* **44**, 2046–2060 (1991).
29. Svetin, D. *et al.* Three-dimensional resistivity switching between correlated electronic states in 1T-TaS$_2$. Preprint at https://arxiv.org/abs/1603.06214 (2016).
30. Darancet, P. *et al.* Three-dimensional metallic and two-dimensional insulating behavior in octahedral tantalum dichalcogenides. *Phys. Rev. B* **90**, 045134 (2014).

The highly correlated quantum phase in 1T-TaS$_2$
M Kratochvilova et al.

7

31. Ma, L. *et al.* A metallic mosaic phase and the origin of Mott-insulating state in 1T-TaS$_2$. *Nat. Comm* **7**, 10956 (2016).

32. Ozaki, H. *et al.* Tunneling investigation of charge density wave energy gap in IT-TaS$_2$. *Phys. B* **117-118**, 590–592 (1983).

33. Noutomi, S. *et al.* Tunneling study of the charge-density-wave state in 1T-TaS$_2$ and 1T-TaSe$_2$. *Solid State Commun.* **50**, 181–184 (1984).

34. Kim, J.-J. *et al.* Observation of Mott Localization Gap Using Low Temperature Scanning Tunneling Spectroscopy in Commensurate 1T-TaS$_2$. *Phys. Rev. Lett.* **73**, 2103 (1994).

35. Stojchevska, L. *et al.* Ultrafast switching to a stable hidden quantum state in an electronic crystal. *Science* **344**, 177–180 (2014).

36. Stewart, J. R. *et al.* Disordered materials studied using neutron polarization analysis on the multi-detector spectrometer, D7. *J. Appl. Cryst.* **42**, 69–84 (2009).